

Shock and Spallation Behavior of a Compositionally Complex High-Strength Low-Alloy Steel under Different Impact Stresses

Ye Lu * and Junbao Li

School of Mechanical Engineering, Nanjing University of Science and Technology, Nanjing 210094, China

* Correspondence: luye@njjust.edu.cn

Abstract: The shock and spalling behavior of a compositionally complex high strength low-alloy steel (HSLA) was studied using plate impact testing. The free surface velocity of the specimen in the range of 194–938 m/s was measured by a displacement interferometer system for any reflector (DISAR). The Hugoniot elastic limit (HEL), spallation fracture and microstructural evolution of the HSLA under an impact stress of 3.04–18.66 GPa were analyzed. Shock Hugoniot curves were obtained from the measured particle velocities and calculated shock velocities. The velocity curves show clear signs of HEL and velocity fallback, indicating a transition from elastic to plastic and spalling behavior. When the impact velocity exceeds 757 m/s, the particle velocity rises to the peak and then increases again, indicating that an $\alpha \rightarrow \epsilon$ phase transition occurred, with a threshold of 13.51 GPa. It was found that the impact velocity is linearly related to the particle velocity of the HSLA. As the impact stress increased, the HEL remained within the range of 1.32–1.50 GPa, while the spalling strength presented an upward trend with the increasing impact stresses. Metallographic analysis shows that the impact failure is dominated by brittle fracture at lower velocities, while more ductile fracture occurs at higher velocities.

Keywords: high-strength low-alloy steel (HSLA); eletroslag remelting (ESR); plate impact test; Hugoniot elastic limit; spall strength



Citation: Lu, Y.; Li, J. Shock and Spallation Behavior of a Compositionally Complex High-Strength Low-Alloy Steel under Different Impact Stresses. *Appl. Sci.* **2023**, *13*, 3375. <https://doi.org/10.3390/app13063375>

Academic Editors: José António Correia and Ana M. Camacho

Received: 30 January 2023
Revised: 24 February 2023
Accepted: 28 February 2023
Published: 7 March 2023



Copyright: © 2023 by the authors. Licensee MDPI, Basel, Switzerland. This article is an open access article distributed under the terms and conditions of the Creative Commons Attribution (CC BY) license (<https://creativecommons.org/licenses/by/4.0/>).

1. Introduction

With the continuous development of low-alloy steel, fine-grained, ultra-fine-grained and other strengthening mechanism technologies, advanced high-strength steels and new high-performance steels have received more and more attention [1–3]. In recent years, high-strength low-alloy steel (HSLA) has been used in engineering components, such as aircraft landing gear and oil pipelines, due to its qualified impact toughness, ultra-high strength and excellent weldability [4–6]. In practical engineering applications, the mechanical properties of 25CrNi high-strength low-alloy steel still need to be improved to withstand greater impact loads directly affected by the operating environment [7].

The metal elements usually added to high-strength low-alloy steels are mainly Ni, Cr, Si, Mn, Mo, V and W [8]. Many scholars add Nb to the composition of C-Mn steel to prepare high-performance HSLA [9,10]. Nb is known to improve the balance of strength and toughness in steel by refining grains. Combined with the corresponding hot rolling and heat treatment processes, the comprehensive properties of the steel can be improved [11]. The microstructure of steel with this composition system is acicular ferrite. Recently, the comprehensive performance requirements of petroleum steel pipes are getting higher and higher, and high-performance petroleum steel pipes have been developed one after another [12]. The formulation of high-strength and high-toughness steel materials whose basic chemical composition system is C, Mn, Cr, Mo and a small number of microalloying elements (such as Nb, V, etc.) has gradually developed [13].

With the improvement of the performance requirements of high-strength and tough steel, along with the development trend of purification in the metallurgical industry, the

requirements for the metallurgical quality of steel are also getting higher and higher [14]. Generally speaking, the residual elements S, P and the five harmful impurity elements Pb, Sb, Bi, Sn, As, etc. in the steel are easy to segregate and precipitate at the grain boundary, and form a low-melting point eutectoid with Fe, which reduces the strength of grain boundaries and affects the hot workability of steel [15,16]. Therefore, it is worthy of attention to reduce the content of impurities, such as S and P, the gas content and the content of nonmetallic inclusions in HSLA, thereby improving the comprehensive mechanical properties of the steel. Electroslag remelting, as a secondary melting technology, can improve the purity of steel and improve the low-magnification structure of steel [17,18]. The REO-MgO-CaO-Al₂O₃-CaF₂ new five-element rare earth slag system was selected, and rare earth deoxidizer was added to the slag pool during the electroslag remelting process to form a certain reducing atmosphere in the electroslag furnace, and finally improve the toughness and toughness of the steel and fatigue performance.

High-strength low-alloy steels provide perfect candidates for major improvements in the automotive, aerospace and military defense fields due to their acceptable impact toughness, ultra-high strength, and excellent weldability [19–21]. In this study, a series of plate impact experiments were carried out to investigate the shock wave structure, HEL and spallation strength in a compositionally complex HSLA. The transition from elastic to plastic behavior under impact flyer loading was analyzed, and the phase transition and spallation of HSLA were determined from the measured free-surface particle velocities and metallographic microscopy of the recovered specimens.

2. Experimental Procedures

2.1. Materials

The experimental HSLA plate was acquired from the Construction Machine Tool Factory (Chongqing, China) and prepared by electroslag remelting, containing the following components: 0.25% C, ~3% Cr, ~2% Mo, ~1% W, ~0.8% Ni ~0.06% V, ~0.06% Nb and balance Fe. In the process of electroslag ingot remelting, CaF₂:Al₂O₃ = 70:30 was used as slag, and it was baked at 800 °C for 6 h before use to fully remove the moisture. In the initial stage of electroslag remelting, graphite electrodes were used to melt lead slag, and slag was continuously added during the process. After the slag has completely melted, replace the consumable electrode. Ar protection was used during the remelting, and SiAlCaBa powder deoxidizer was used throughout the process. The density of the HSLA was measured as $7.76 \pm 0.03 \text{ g/cm}^3$. The longitudinal, shear, and bulk sound speeds (c_L , c_S and c_B , respectively) are shown in Table 1. A typical scanning electron micrograph of the HSLA is shown in Figure 1. It is shown that the matrix structure is mainly martensite with a small amount of tempered sorbite, and the fine carbide particles are distributed between the lath and the grain boundary.

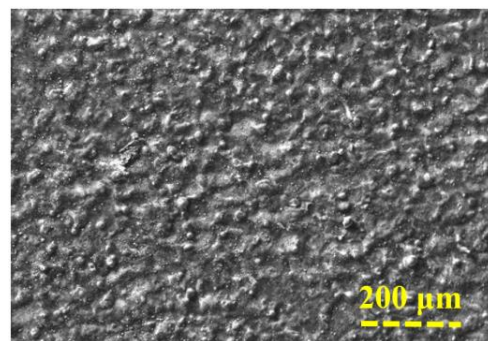


Figure 1. Microstructure images of the HSLA.

Table 1. Material properties of the HSLA.

Material	ρ_0 (g/cm ³)	c_L (m/s)	c_S (m/s)	c_B (m/s)
Cr-Mo-W-Ni-V-Nb steel	7.76 ± 0.03	5213	3308	4029

2.2. Plate-Impact Test

The schematic diagram of the plate impact experiment is shown in Figure 2. The test device is composed of a loading system, test target and test system. The loading system consists of a 37-mm-diameter air gun, a 4-m-long high-pressure chamber, a cartridge case and an oxygen-free high conductivity (OFHC) flyer plate (35 mm in diameter \times 1.5 mm in diameter). By adjusting the driving pressure and the size and mass of the shell, the impact velocity of the shell flight, the flight balance of the shell and the impulse width of the shock wave in the target can be controlled. The target plate is composed of a specimen (15 mm in diameter \times 3 mm in diameter) and an epoxy resin filler. The test system is composed of a trigger device, a signal processing device and an arbitrary mirror displacement interferometer system.

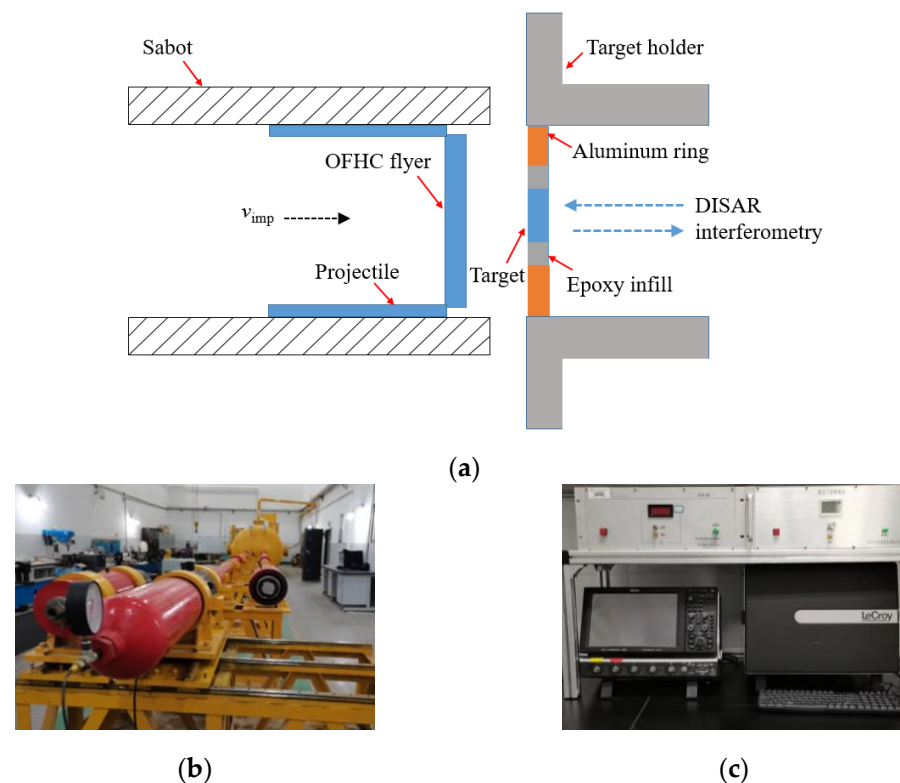


Figure 2. Schematic illustration of the plate impact experiments for the HSLA. (a) schematic diagram; (b) image of air gun; (c) image of DISAR.

During the test, pressurized hydrogen gas was used to accelerate the flyer, located in front of the stock, towards the target, a series of charged metal pins were used to measure the impact velocity, v_{imp} . The velocity distribution of the free surface on the backside of the target specimen was directly measured using a fiber optic probe, and the shock wave velocity of the specimen was obtained through a point probe and an optical window. In order to eliminate the influence of installation error and impact nonuniformity, the electrical probes were arranged at each of the four corners of the sample target so that the end faces were flush with the impact surface of the sample. When the flyer is 0.5 mm away from the target, both the pin and DISAR are triggered at time zero t_0 . DISAR monitors the shock wave passing through the target on the free surface of the target. The specific test scheme is shown in Table 2. To reveal the impact response and spalling behavior of HSLA

at different impact velocities from a microscopic perspective, a metallographic analysis of the recovered specimens was performed after cutting, grinding, polishing and etching using an Axio Imager Mim optical microscope.

Table 2. Experimental details of the plate impact test.

Test No.	Impact Velocity v_{imp} (m/s)	Thickness (mm)		Diameter (mm)	
		Specimen	OFHC	Specimen	OFHC
001	194	2.960	1.497	14.99	34.97
002	409	3.051	1.480	14.95	34.95
003	410	3.055	1.480	14.99	34.95
004	598	3.030	1.479	15.02	35.02
005	782	3.051	1.487	15.01	35.01
006	858	3.040	1.497	15.00	34.96
007	938	3.050	1.488	15.02	34.95

3. Results and Discussion

3.1. Gauge Trace Analyses

Regarding the free surface velocity distribution, some typical characteristics should be noted: When the elastic precursor wave reaches the free surface of the sample, the free surface particle velocity increases sharply to a certain value, which can be used to calculate the HEL value; when damage or spalling occurs in the sample, the sparse waves are reflected as compressional waves in damaged or denuded regions, resulting in an early pullback of the free surface velocity, which can be used to estimate spall strength under the assumption of an acoustic approximation; the Hugoniot relationship of the specimen can be determined from particle velocity, impact velocity, and impact stress.

Figure 3 shows the free surface velocity of test sample No. 004 monitored by DISAR. To illustrate shock wave propagation more clearly, a graph of Lagrangian distance versus time is shown and the timescale of the x -axis is canceled in Figure 3. The specimen was initially impacted by the OFHC flyer at time t_0 , producing an elastic precursor (dashed line) and a shock wave (solid line) in the specimen and flyer. It is assumed that the elastic precursor propagates at the longitudinal speed of sound c_L , which is faster than the speed of the shock wave. Therefore, the precursor wave reaches the rear free surface of the specimen at time t_1 , resulting in a rapid increase in particle velocity in a very short time (a measurement value less than 15 ns). It is clear from the free surface velocity curve that the particle velocity increases linearly with HEL. The HEL is followed by distortion of the elastic-plastic yielding and free-surface velocity data due to the time period during which the elastic precursor reflects back to the oncoming shock wave and the interaction that occurs between the different stress pulses. Thereafter, the shock wave, propagating at the velocity U_s , reached the free surface at the rear of the specimen at time t_2 . The arrival of the shock wave caused the free surface velocity to rapidly increase to a peak value.

Once the shock wave reached the flyer and the free surface of the specimen, it was reflected back as a rarefaction wave. It is well known that the head of the release wave also propagated at the longitudinal sound speed, while the tail of the release wave propagated at the bulk sound speed. Measurements of the above parameters for the HSLA are given in Table 1. When the rarefaction waves from the free surface of the specimen and OFHC met at time t_3 , a tensile stress was generated. When the tensile stress exceeds its spall strength, a free surface appears on the spall surface, and a pulse propagating at the longitudinal speed of sound is generated on the surface. The pulse reached the rear free surface of the specimen at time t_4 , resulting in a reduction in velocity. A new pulse arrived at time t_5 and caused a characteristic pullback in the velocity, which is further evidence of the occurrence of spallation. The change in free surface velocity between the peak and the first minimum is called the pullback velocity, which is used to calculate the spalling strength of the material. As shown in Figure 3, the smaller peak after the free surface velocity maximum is due to the spallation pulse propagating back and forth within the surface after failure.

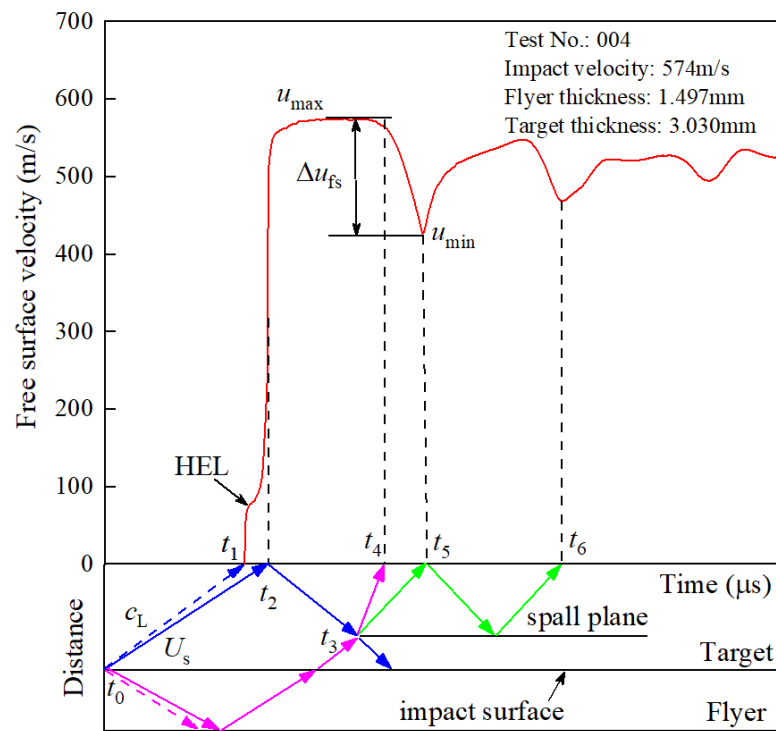


Figure 3. Representative free surface velocity in test No. 004 under impact loading.

Figure 4 presents the measured back-free surface velocity curves for all specimens at flyer impact velocities ranging from 194 to 938 m/s, each of which indicates the transition from elastic to plastic deformation. As can be seen, the free surface velocity at the HEL varies very little, ranging from approximately 65.5 to 74.0 m/s. Unlike HEL, the trend in pullback velocity is more complex, and the details of spall strength are quantified and discussed in Section 3.3. It should be noted that the slope curve increases significantly after velocity pullback, which is believed to be related to the change in the failure mode of the material from brittle to more ductile [22].

It can be also observed in Figure 4 that the change in particle velocity curves at higher impact velocities (782 m/s, 858 m/s and 938 m/s), i.e., another step change in particle velocity occurred at the peak platform. As the peak stress (σ_{peak}) increased to the phase transition stress threshold, the $\alpha \rightarrow \epsilon$ phase transition occurred and a phase-transition pulse was generated, resulting in a transformation of the particle velocity profile from a two-wave structure to a three-wave structure, consisting of elastic, plastic and phase transition waves. Referring to the method used by Boteler and Dandekar [23], the peak stress was determined using the peak free surface velocity (u_{pfs}), the shock velocity (U_s for elastic waves and U_p for plastic waves) and density. According to the Rankine–Hugoniot relationships, the stress threshold for the $\alpha \rightarrow \epsilon$ phase transition was calculated as 13.51 GPa.

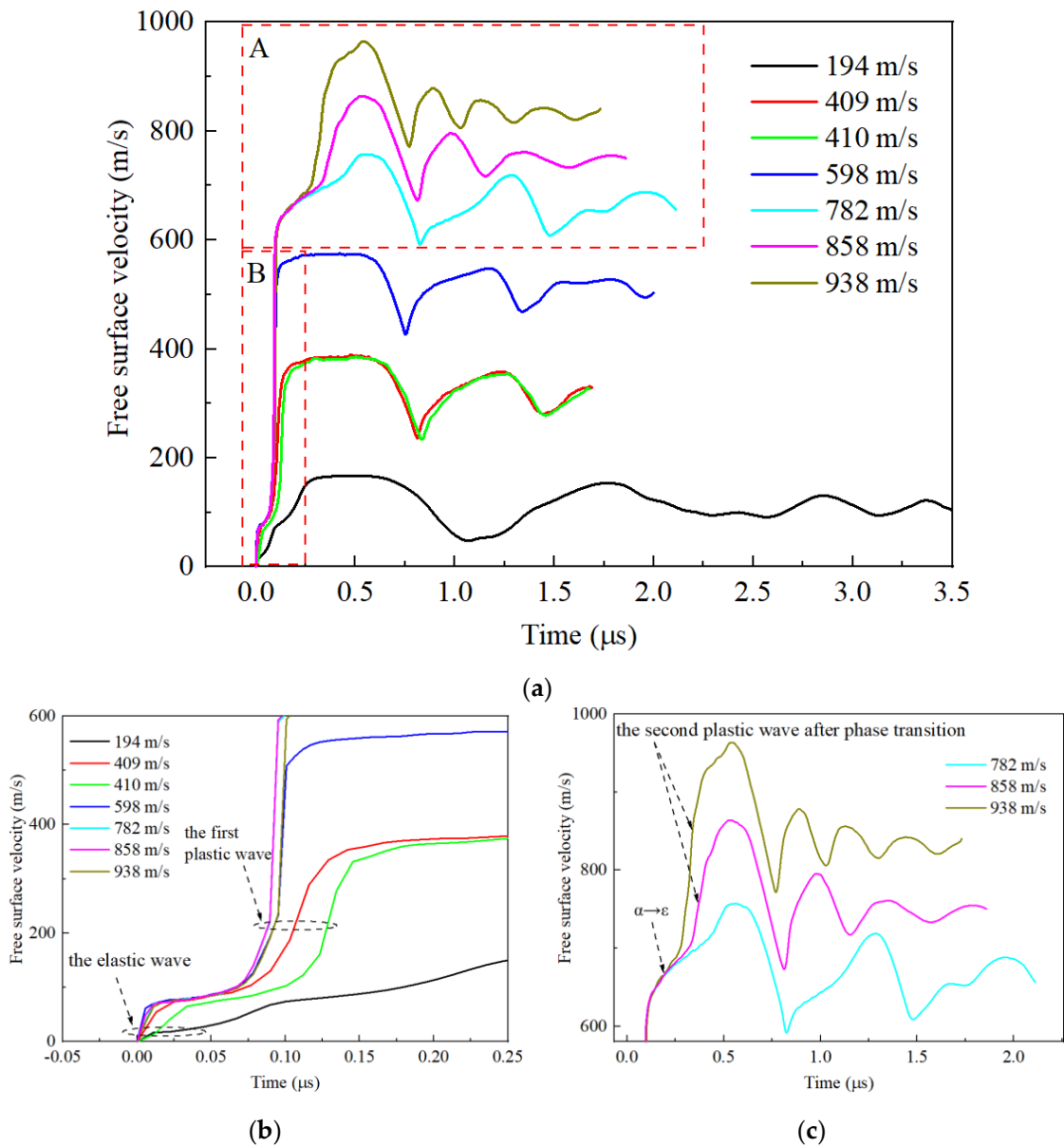


Figure 4. Rear free surface velocity vs. time for all specimens at flyer impact velocities from 194 to 938 m/s. (a) measured curves; (b) zone A; (c) zone B.

3.2. Hugoniot Elastic Limit and Spall Strength

In these experiments, the Hugoniot elastic limit, σ_{HEL} , and spall strength, σ_{spall} , of the HSLA were determined by the measured free surface velocity data, which can be expressed as:

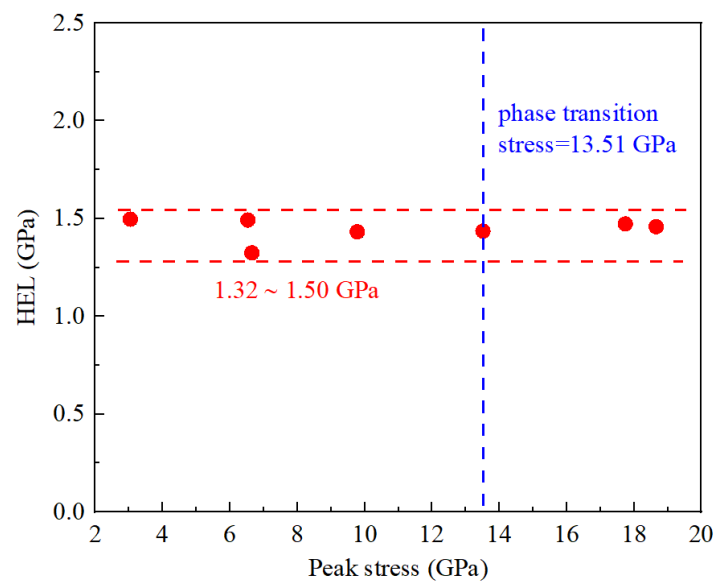
$$\sigma_{HEL} = \frac{1}{2} \rho_0 c_L u_e \tag{1}$$

$$\sigma_{spall} = \frac{1}{2} \rho_0 c_0 \Delta u_{fs} \tag{2}$$

where the density ρ_0 and sound speeds c_L and c_0 are known, and u_e and Δu_{fs} can be calculated according to the measured HEL and pullback velocity. The calculated HEL and spallation strengths are listed in Table 3. As is shown in Figure 5, the stress at the HEL of the HSLA is estimated to be in the range of 1.32~1.50 GPa, presenting a similar HEL when compared with that of other conventional crystalline alloys [24,25], such as mild steel (1.75 GPa), austenitic stainless steel (1.40 GPa) and HY80 naval armor steel (1.70 GPa).

Table 3. Experimental results for the HSLA obtained by plate impact test.

Test No.	u_{pfs} (m/s)	U_s (m/s)	u_e (m/s)	σ_{HEL} (GPa)	σ_{peak} (GPa)	Δu_{fs} (m/s)	σ_{spall} (GPa)	$\dot{\epsilon}$ ($10^3 s^{-1}$)
001	168	4023	74.0	1.50	3.04	120.0	1.88	33.2
002	384	4179	73.8	1.49	6.53	147.5	2.31	66.6
003	382	4273	65.5	1.32	6.65	147.8	2.31	78.1
004	574	4480	70.8	1.43	9.78	147.3	2.30	81.6
005	757	4525	71.0	1.44	13.51	165.5	2.59	81.5
006	864	4577	72.8	1.47	17.74	191.3	2.99	100.6
007	984	4579	72.1	1.46	18.66	212.2	3.32	120.2

**Figure 5.** Calculated HEL values for the HSLA.

The above analysis shows that the HSLA will be pulled by the rarefaction wave from the free surface of the specimen and OFHC, generating a pullback zone on the free surface velocity curve. Two important characteristics of this stage are the pullback speed and pullback amplitude: the former is related to the tensile strain rate, while the latter directly determines the peeling strength of the HSLA. The tensile strain rate can be calculated using Equation (3):

$$\frac{d\epsilon}{dt} = \frac{1}{2} \frac{du_{fs}}{c_0 dt} \quad (3)$$

Table 3 shows the calculated values of the tensile strain rate at the impact velocities from 194 m/s to 938 m/s, which are in the range of $33.2 \times 10^3 \sim 120.2 \times 10^3 s^{-1}$, as shown in Figure 6. It is observed that the HSLA has high spallation strength (1.88~3.32 GPa) when compared with other steels [24,26], such as Armco iron (1.07 GPa) and 09G2S steel (0.7~1.4 GPa). Below the phase-transition stress, the spallation strength first increased and then decreased with increasing shock stresses. This trend is attributed to the accumulation of damage within the HSLA as the initial shock-induced compression wave propagates, revealing that larger shock stress leads to a larger damage magnitude. Generally speaking, the spalling strength is related to the microstructure, the propagation of the impact pulse and the damage to the material. Differences in the time-sensitivity of damage initiation and propagation may cause variations in spall strength: when the material is loaded at higher strain rates, dynamic loading does not have enough time to induce internal defects in the material, resulting in a decrease in the spallation strength.

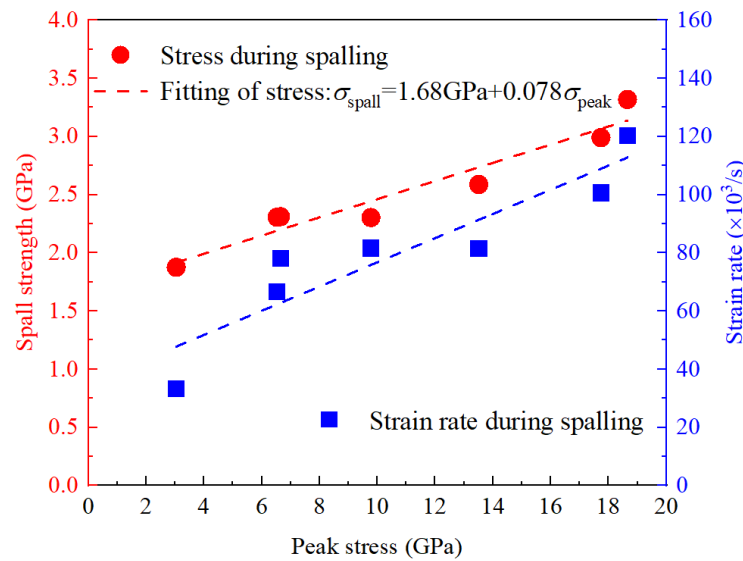


Figure 6. Calculated values of spallation strength and tensile strain rate at different impact velocities for the HSLA.

When the impact stress is increased to the $\alpha \rightarrow \epsilon$ transformation stress, an increase in the rate of increase in spallation strength is observed. In general, the phase transformation of the alloy occurs before the spallation behavior, and the microstructure produced by the phase transformation will directly affect the subsequent tensile fracture of the material. Therefore, the apparent increase in the spallation strength may be due to the massive movement of dislocations in the internal lattice of the material after undergoing a phase transition, resulting in material hardening.

3.3. Hugoniot Relationships

From the measured particle velocity profile, the shock velocity can be calculated using the longitudinal elastic wave velocity (c_L), taking the amount of deformation as a reference value, and using the time of the plastic part of the shock wave front between the elastic limit and the peak free surface velocity, by:

$$U_s = \frac{d}{\frac{d}{c_L} + \Delta t} \tag{4}$$

where d is the thickness of the specimen. According to the free surface reflection multiplication law [27], the particle velocity inside the material is half of the back-free surface velocity. The Hugoniot data for HSLA in the impact velocity (U_s)-particle velocity (u_p) space are shown in Figure 7. The obvious linear relationship was fitted to a linear equation given by:

$$U_s = c_0 + Su_p \tag{5}$$

where c_0 is the zero-pressure bulk sound velocity and S is the slope, which is related to the first derivative of the bulk modulus with pressure [28].

As shown in Figure 7, the shock parameters $c_0 = 3961$ m/s and $S = 1.415$ for the HSLA were determined. Data on pure iron obtained from references were also provided [10]. Compared to pure iron, the S value in our data is smaller, with a deviation of 15.7%. Considering that a lower value of S means greater resistance to compressive deformation [28], the improvement in stiffness of the HSLA may be due to the addition of other metal elements.

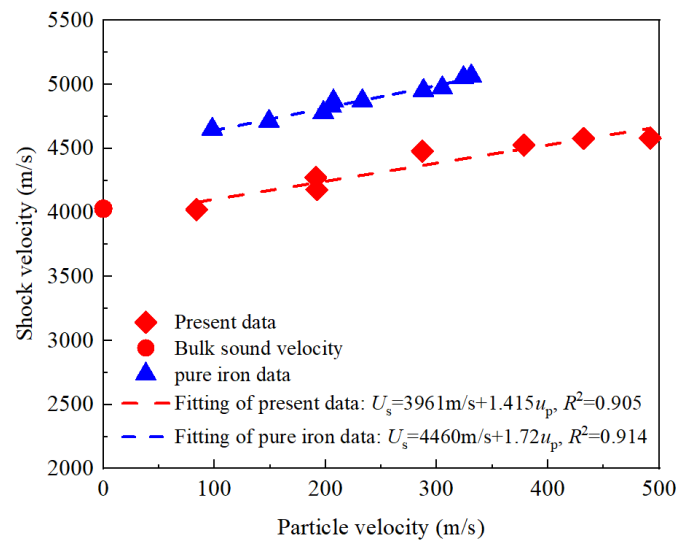


Figure 7. Shock velocity-particle velocity relationship for the HSLA, along with data for pure iron from Thomas et al. [10].

3.4. Microscopic Analysis

Figure 8 shows the macroscopic and microscopic failure modes of all recovered specimens at different impact velocities processed by wire cutting. It can be seen that microvoids induced by the shock loading appeared in the specimen when it impacted at a velocity of 409 m/s, which may significantly affect the shock wave propagation and spalling behavior of the HSLA. When the impact velocity was increased to 938 m/s, the HSLA presented obvious plastic deformation, and a significant tensile failure occurred inside the material.

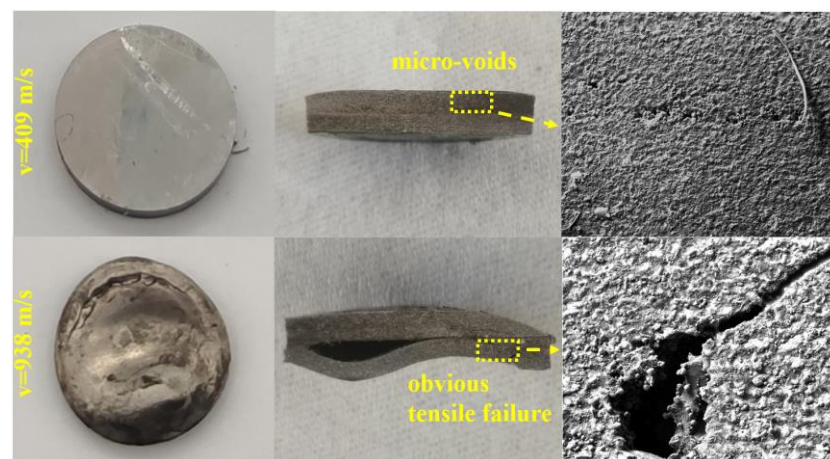


Figure 8. Macro- and microfailure modes of all recovered test specimens under different impact velocities.

After testing under impact-induced compressive and tensile loads, the fractured surfaces of the recovered samples were examined by metallographic microscopy. Figure 9 shows the metallographic microscopy observations of the internal structure of the recovered specimens at impact velocities of 409 m/s and 938 m/s. Significant lamellar cracks were observed in both specimens. The 409 m/s sample showed higher crack density and multiple spalling layers, and more microvoids can be observed near the surface of the spalling layers. It is well known that the ductile-dynamic tensile failure of metals is controlled by three stages of microscopic processes, such as void nucleation, void growth, and eventual fracture through void mergers. The interface between different types of grains can become the nucleation position of voids and the crack tip, resulting in the material showing greater

spallation strength at the impact speed of 598 m/s. In contrast, the failure mode along the impact direction is clearer at 938 m/s, which exhibits the larger crack length and crack opening as well as the lower crack density. From the perspective of phase transformation, the HSLA exhibits spalling characteristics at low impact velocities similar to most alloy steels. At the higher impact velocity of 938 m/s, due to the dislocation movement in the internal lattice after the material undergoes phase transformation, the possibility of multilayer failure under impact stress is also reduced.

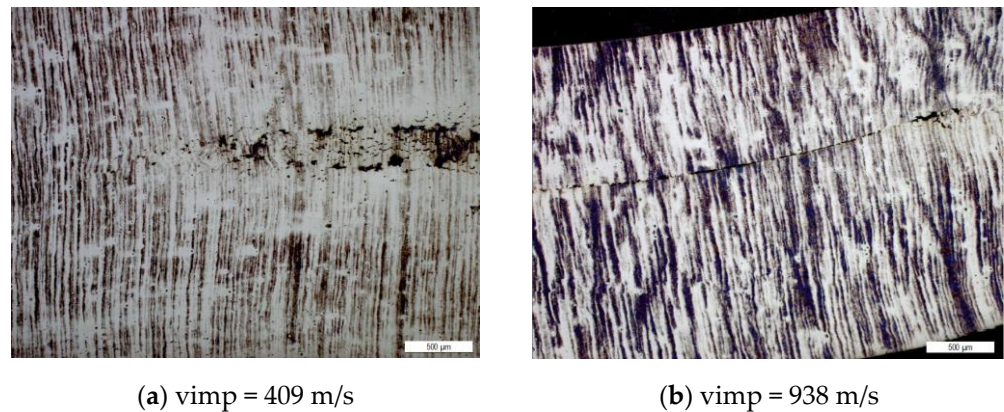


Figure 9. Metallographic microscope observation of internal structures of recovered specimens subjected to impact velocities of 409 m/s and 938 m/s.

4. Conclusions

The shock-compression response and spalling behavior of a high-strength low-alloy steel with a complex composition were studied. The free surface velocity curve of the HSLA under impact stress in the range of 3.04~18.66 GPa was measured, and the metallographic analysis of the recovered specimens was carried out. This study can lay the foundation for the development of high-performance alloy steel and promote its application in large construction machinery, aircraft missile casings, armored tank vehicle structures, and protective materials. The main conclusions are as follows:

- (1) The entire mechanical behavior of the HSLA under the loading of the plate impact was investigated based on the free surface velocity, from initial elastic deformation to plastic deformation caused by the shock wave, and then to the spalling process under the interaction of the rarefaction wave. When the impact velocity exceeded 757 m/s, an $\alpha \rightarrow \epsilon$ phase transition occurs within the material that causes a step change in the particle velocity. The calculated phase-transition stress threshold is 13.51 GPa.
- (2) The shock wave velocity and shock stress of the HSLA were calculated based on the measured particle velocity. It is found that an obvious linear relationship exists between the shock wave velocity U_s and the particle velocity u_p : $U_s = 3961 \text{ m}\cdot\text{s}^{-1} + 1.415 u_p$.
- (3) It is found that the HEL of the HSLA exhibited little change with an increase in impact stress, remaining consistent within the range of 1.32~1.50 GPa. The strain rate and spallation strength first increased and then decreased because of the high strain rate. The spallation strength increased again after the phase transformation, which may be related to microstructural changes caused by the phase transformation.
- (4) Microscopic observation of recovered specimens showed that the HSLA exhibited multiple spalling layers under low-velocity impact and that the failure mode was mainly a brittle fracture. Under high-velocity impact, the crack opening was larger and clearer, and the failure mode changed from an initial brittle fracture mechanism to a more ductile fracture mechanism.

Author Contributions: Conceptualization, Y.L. and J.L.; investigation, Y.L. and J.L.; writing—original draft preparation, Y.L.; writing—review and editing, Y.L. and J.L. All authors have read and agreed to the published version of the manuscript.

Funding: The work presented in this paper was funded by the Innovation Special Zone Project of the Science and Technology Commission of the Military Commission (grant number 22-TQ01-04-ZT-01-009) and the China Postdoctoral Science Foundation (grant number 2018T110503).

Institutional Review Board Statement: Not applicable.

Informed Consent Statement: Not applicable.

Data Availability Statement: The data presented in this study are available on request from the corresponding author upon reasonable request.

Conflicts of Interest: The authors declare no conflict of interest.

References

1. Chen, C.; Zhang, F.C.; Yang, Z.N.; Zheng, C.L. Superhardenability behavior of vanadium in 40CrNiMoV steel. *Mater. Des.* **2015**, *83*, 422–430. [[CrossRef](#)]
2. Zhu, M.L.; Liu, L.L.; Xuan, F.Z. Effect of frequency on very high cycle fatigue behavior of a low strength Cr–Ni–Mo–V steel welded joint. *Int. J. Fatigue* **2015**, *77*, 166–173. [[CrossRef](#)]
3. Wu, W.; Zhu, M.L.; Liu, X.; Xuan, F.Z. Effect of temperature on high-cycle fatigue and very high cycle fatigue behaviours of a low-strength Cr–Ni–Mo–V steel welded joint. *Fatigue Fract. Eng. Mater. Struct.* **2017**, *40*, 45–54. [[CrossRef](#)]
4. Yang, Y.; Fan, L.; Xu, C.; Dong, X. Experimental Study of Mechanical Properties of 30SiMn2MoVA Steel Gun Barrel Processed by Cold Radial Forging. *J. Press. Vessel. Technol.* **2021**, *143*, 011501. [[CrossRef](#)]
5. Keeler, S.; Kimchi, M.; Mooney, P.J. Advanced high-strength steels application guidelines version 5.0. *World Auto Steel* **2014**, 276.
6. Matlock, D.K.; Speer, J.G. Third generation of AHSS: Microstructure design concepts. In *Microstructure and Texture in Steels*; Springer: London, UK, 2009; pp. 185–205.
7. Du, Y.F.; Lu, H.H.; Shen, X.Q. Coupled effects of banded structure and carbide precipitation on mechanical performance of Cr–Ni–Mo–V steel. *Mater. Sci. Eng. A* **2022**, *832*, 142478. [[CrossRef](#)]
8. Lesuer, D.R.; Syn, C.K.; Sherby, O.D. Physical Metallurgy and the Design of Steels Physical Metallurgy and the Design of Steels, 1978. *Mater. Trans.* **2006**, *47*, 1508–1517. [[CrossRef](#)]
9. Dutta, B.; Sellars, C.M. Effect of Composition and Process Variables on Nb(C, N) Precipitation in Niobium Microalloyed Austenite. *Mater. Sci. Technol.* **1987**, *3*, 197–206. [[CrossRef](#)]
10. Miao, C.; Shang, C.; Zhang, G.; Subramanian, S.V. Recrystallization and Strain Accumulation Behaviors of High Nb-Bearing Line Pipe Steel in Plate and Strip Rolling. *Mater. Sci. Eng. A* **2010**, *527*, 4985–4992. [[CrossRef](#)]
11. Hong, S.G.; Jun, H.; Kang, K.B.; Park, C.G. Evolution of Precipitates in the Nb-Ti-V Microalloyed HSLA Steels During Reheating. *Scr. Mater.* **2003**, *48*, 1201–1206. [[CrossRef](#)]
12. Sha, Q.; Sun, Z. Grain Growth Behavior of Coarse Grained Austenite in a Nb-V-Ti Microalloyed Steel. *Mater. Sci. Eng. A* **2009**, *523*, 77–84. [[CrossRef](#)]
13. Bai, D.; Yue, S.; Maccagno, T.; Jonas, J.J. Effect of Deformation and Cooling Rate on the Microstructures of Low Carbon Nb-B Steels. *ISIJ Int.* **1998**, *38*, 371–379. [[CrossRef](#)]
14. Rao, L.; Zhao, J.; Zhao, Z.; Ding, G.; Geng, M.P. Macro-and microstructure evolution of 5CrNiMo steel ingots during electroslag remelting process. *J. Iron Steel Res. Int.* **2014**, *21*, 644–652. [[CrossRef](#)]
15. Ju, J.; Ji, G.; Tang, C.; Yang, K.; Zhu, Z. The effect of Li₂O on the evaporation and structure of low-fluoride slag for vacuum electroslag remelting. *Vacuum* **2021**, *183*, 109920. [[CrossRef](#)]
16. Kharicha, A.; Karimi-Sibaki, E.; Wu, M.; Ludwig, A.; Bohacek, J. Review on modeling and simulation of electroslag remelting. *Steel Res. Int.* **2018**, *89*, 1700100. [[CrossRef](#)]
17. Arh, B.; Podgornik, B.; Burja, J. Electroslag remelting: A process overview. *Mater. Technol.* **2016**, *50*, 971–979. [[CrossRef](#)]
18. Weber, V.; Jardy, A.; Dussoubs, B.; Ablitzer, D.; Rybérón, S.; Schmitt, V.; Hans, S.; Poisson, H. A comprehensive model of the electroslag remelting process: Description and validation. *Metall. Mater. Trans. B* **2009**, *40*, 271–280. [[CrossRef](#)]
19. Wilkerson, J.W.; Ramesh, K.T. A dynamic void growth model governed by dislocation kinetics. *J. Mech. Phys. Solids* **2014**, *70*, 262–280. [[CrossRef](#)]
20. Meyers, M.A.; Staudhammer, K.P.; Murr, L.E. (Eds.) *Metallurgical Applications of Shock-Wave and High-Strain-Rate Phenomena*; Marcel Dekker: New York, NY, USA, 1986.
21. Chen, X.; Asay, J.R.; Dwivedi, S.K.; Field, D.P. Spall behavior of aluminum with varying microstructures. *J. Appl. Phys.* **2006**, *99*, 023528. [[CrossRef](#)]
22. Whelchel, R.L.; Kennedy, G.B.; Dwivedi, S.K.; Sanders, T.H., Jr.; Thadhani, N.N. Spall behavior of rolled aluminum 5083-H116 plate. *J. Appl. Phys.* **2013**, *113*, 233506. [[CrossRef](#)]
23. Brar, N.S.; Rosenberg, Z. Shock Hugoniot of 1215 steel. *AIP Conf. Proc.* **1996**, *370*, 101–104.
24. Wang, G.Y. Influence of Shock Pre-Compression Stress and Tensile Strain Rate on the Spall Behaviour of Mild Steel. *Strain* **2011**, *47*, 398–404. [[CrossRef](#)]
25. Brown, J.M.; Fritz, J.N.; Hixson, R.S. Hugoniot data for iron. *J. Appl. Phys.* **2000**, *88*, 5496–5498. [[CrossRef](#)]

26. Ogorodnikov, V.A.; Borovkova, E.Y.; Erunov, S.V. Strength of some grades of steel and armco iron under shock compression and rarefaction at pressures of 2–200 GPa. *Combust. Explos. Shock. Waves* **2004**, *40*, 597–604. [[CrossRef](#)]
27. Meyers, M.A. *Dynamic Behavior of Materials*; John Wiley & Sons Inc.: Hoboken, NJ, USA, 1994.
28. Davison, L.; Graham, R.A. Shock compression of solids. *Phys. Rep.* **1979**, *55*, 255–379. [[CrossRef](#)]

Disclaimer/Publisher’s Note: The statements, opinions and data contained in all publications are solely those of the individual author(s) and contributor(s) and not of MDPI and/or the editor(s). MDPI and/or the editor(s) disclaim responsibility for any injury to people or property resulting from any ideas, methods, instructions or products referred to in the content.